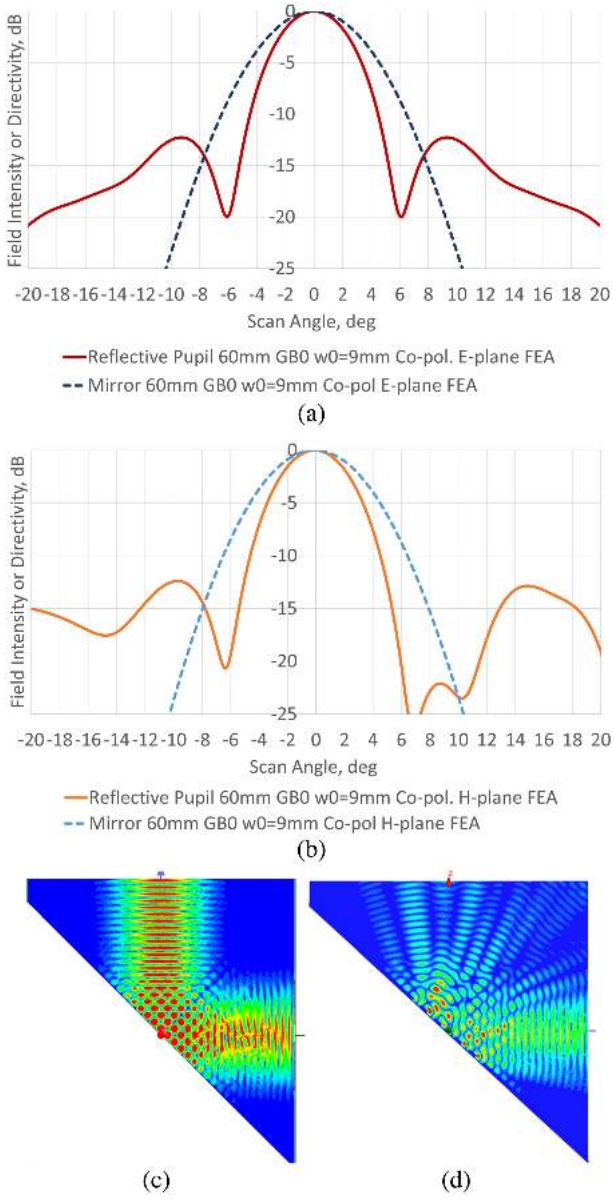

Fig. 6. Finite-element simulation results at 100 GHz of the reflective pupil [Fig. 5(a)] illuminated by an ideal Gaussian beam with a 9 mm beam waist at the center of the pupil: (a) E-plane beam patterns of the Gaussian beam reflected from the embedded unpatterned mirror and from the pupil pattern; (b) same in the H plane; (c) and (d) are the electric near-field amplitude distributions for the mirror and pupil, respectively.

The simulations at 100 GHz in Fig. 6 demonstrate ∼25% reduction of the FWHM by the pupil as compared with the reflection from the 60 mm diameter PEC mirror, as well as SLL < -11 dB in both the H and E planes. The asymmetry of the sidelobes in the H plane [Fig. 6(b)] has a fundamental nature and can be qualitatively demonstrated using the Kirchhoff diffraction equation for a slit or an annular aperture illuminated by a beam at oblique incidence [27]. The Fresnel diffraction model employed in our analysis and design constitutes a simplified version of the Kirchhoff formula in the case when the diameter of the aperture is much larger than the wavelength. Nevertheless, it suits the purpose of the design and provides sufficient accuracy within limited angular range, given after all that the final optimization of the structure is carried out by FEA simulation. Anyway, the results in Fig. 6 correspond well with the design values obtained with the first-order diffraction model.

3. FABRICATION AND OPTICAL CHARACTERIZATION

A. Reflective Toraldo Pupil Fabrication

The reflective pupil device was manufactured using the Cardiff University multilayer heat-bonding technology. The pupil pattern was fabricated by photolithographic process using 400 nm evaporated copper film on a 10 um PP carrier substrate. The pupil pattern layer was sandwiched between the pPTFE substrate and PP superstrate using 6 um low-density polyethylene (LDPE) as the bonding film. A solid 400 nm copper back-short was added as well. The assembly was hot-pressed using a special thermal cycle to prevent warping, and the fabricated device is shown in Fig. 7. Although the outer diameter of the fabricated pupil was 200 mm, that was expected to have indiscernible effect as compared to the simulated 60 mm device, due to the relatively small Gaussian beam width.

The flatness of the reflective device proved to be imperative for accurate optical characterization, so that special care was taken during the fabrication and measurements. Upon visual examination, it appeared that the pPTFE substrate imparted subwavelength roughness on the embedded conductor as well as on the back-short. However, comparison of the reflection from the rough back-short and from a reference smooth copper mirror suggested negligible impact of such roughness on the measurement. Therefore, we inferred that the effect of the roughness of the embedded interfaces (viz., PP–copper, PP–pPTFE, and pPTFE–copper) on the reflection was insignificant.

B. Experimental Setup

The fabricated reflective Toraldo pupil device was measured at 45° off-axis incidence using an automated beam-scanning test bench (Fig. 8). The test setup features a quasi-optical (QO)

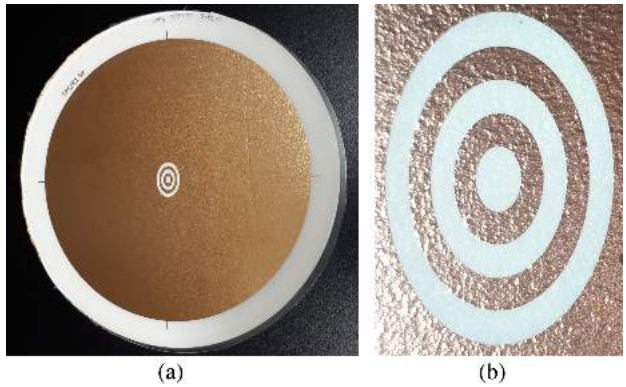

Fig. 7. Fabricated reflective Toraldo pupil prototype: (a) full top-view of the device showing the elliptical inner coronae; (b) close-up view on the inner coronae pattern.

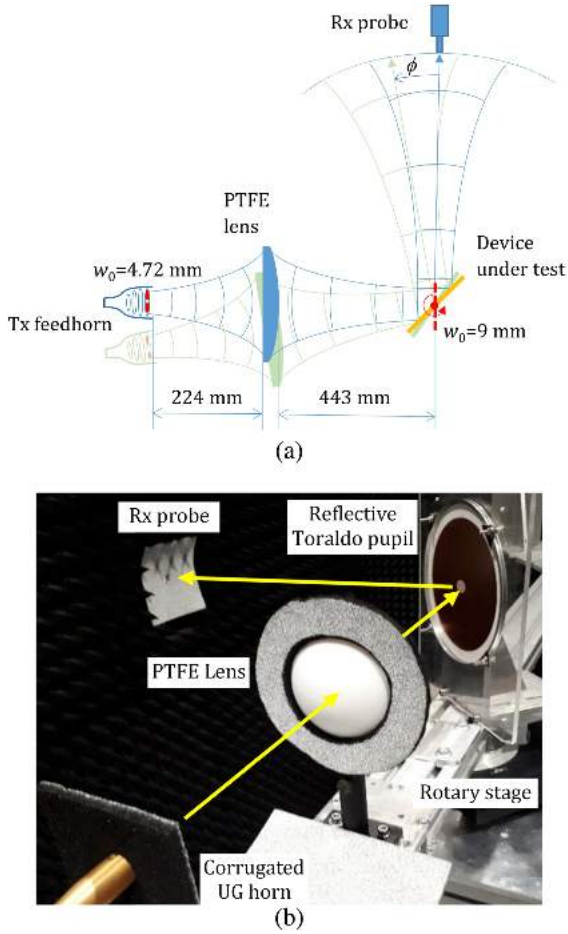

Fig. 8. Quasi-optical test bench for characterization of the reflective Toraldo pupil device: (a) optical sketch (top view) of the beam-measurement setup, with ϕ representing the scan angle as per Eq. (1); (b) photograph of the device being measured. [Figure 8(b) shows the test bed being assembled with the convex side of the lens facing the source feed horn, although it was rotated and facing the DUT, c.f., Fig. 8(a), in actual measurements.]

feed chain comprising a W-band corrugated feed horn, [28], emitting an ultra-Gaussian (UG) beam (Ultra-Gaussian horns feature higher power conversion into the fundamental mode and lower sidelobes as compared to the conventional horns, which is achieved by adding H_{1n} modes to the principal H_{11} mode.) of linear polarization and a commercial plano-convex PTFE lens (Thorlabs LAT151) transforming the source beam waist into a larger beam at the center of the pupil.

Following the analysis based on the Gaussian beam transformation by a thin lens [29], the lens was placed at 224 mm from the horn aperture with its plane side facing the incident wave, since the incident beam has a smaller radius of curvature as compared with the outgoing beam. The device under test (DUT) was set vertically at 45° to the beam axis at 443 mm distance from the vertex of the lens. The major axes of the concentric elliptical coronae of the reflective Toraldo pupil were oriented horizontally so that the patterned aperture effectively appeared circular when projected onto the plane orthogonal to the beam axis. This arrangement was aimed to fit the source beam within the PTFE lens aperture while providing a suitable beam waist on the Toraldo pupil aperture. Both distances were fine-tuned for minimum phase variation versus scan angle across the main beam, although no true phase center was found.

The rotating scan was implemented with a precision rotary motor operated by a motion controller. The transmission parameter measurements were carried out in the high W-band (88-110 GHz) using commercial Rohde & Schwarz ZVA-67 vector network analyzer (VNA) equipped with ZVA-Z110 frequency converters. At each angular position of the scan, the data readings were taken twice in both forward and reverse rotation directions, which allowed *in situ* monitoring of the effects of RF noise and rotational backlash (rotor slip) and thus ensured the best quality data. The experiment was conducted inside an anechoic chamber, and attention was given to terminate the main beam when it was not pointing to the receiver probe (a custom-designed W-band matched the open-ended circular waveguide feed with 2.39 mm aperture). The VNA and motion controller were integrated into the automated measurement system with the aid of LabView software and National Instruments GPIB interface cards (Fig. 9).

The stand-alone source feed horn was characterized by FEA simulation and beam-pattern measurement, and its beam waist retrieved from the FWHM at 100 GHz was 4.72 mm, corresponding to ∼0.59 of the aperture radius and thus indicating a lower aperture illumination efficiency of the UG horn as compared to the conventional conical corrugated horns. The ultra-Gaussian beams also feature high-order modes [30]. Therefore, special consideration was given to characterization of the source beam Gaussicity, which might have had undesirable, possibly unpredictable, effect on the modal purity of the lens-transformed beam illuminating the pupil, which thus undermined the comparison of the simulations with the measurement.

Putting aside the beam vorticity, a circularly symmetric beam profile can be decomposed into a superposition of Laguerre–Gaussian modes in cylindrical coordinates [30] as follows:

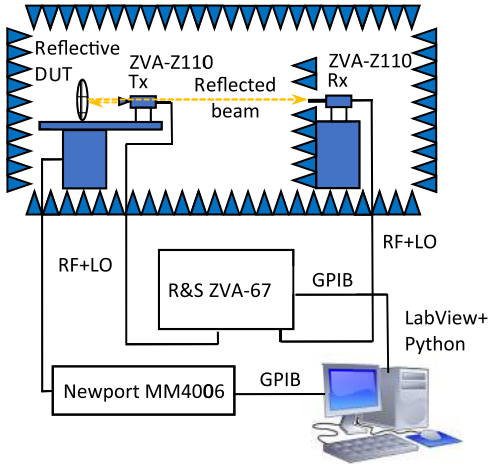

Fig. 9. Schematic diagram of the automated beam-pattern measurement system for reflective pupil characterization.

$$U(r,z)=\sum_p C_p\cdot\sqrt{\frac{2}{\pi}}\cdot\frac{w_0}{w(z)}\cdot\exp\left(-\frac{r^2}{w(z)^2}\right)\cdot L_p\left(\frac{2\cdot r^2}{w(z)^2}\right)$$
$$\cdot\exp\left(-\frac{i\cdot k\cdot r^2}{2\cdot R(z)}\right)\cdot\exp\left(i\cdot\theta_p(z)\right),\quad(3)$$

where C_p is the complex amplitude of the mode with index p and $L_p(\cdots)$ is the corresponding Laguerre polynomial.

The Gaussian beam in Eq. (3) is defined by the radius of curvature of the spherical wavefront $R(z)$, the Rayleigh range z_R, and the beam width along the direction of propagation $w(z)$, given as [29,30]

$$R(z)=z\cdot\left[1+(z_R/z)^2\right];$$
$$z_R=\pi w_0^2/\lambda;$$
$$w(z)=w_0\cdot\sqrt{1+(z/z_R)^2}.$$

The Gouy phase shift of the pth mode in Eq. (3) is given by

$$\theta_p(z)=2\cdot p\cdot\mathrm{a\,tan}(z/z_R).$$

The beam generated by the standalone UG horn (measured directly) and that transformed by the QO feed network were characterized using Eq. (3). In the modeling, we kept the number of polynomial terms to a minimum and the respective coefficients real valued, when possible, to fit the measured data with reasonable accuracy. A constraint on the polynomial coefficients was imposed by requiring the model beam to have the same beam waist at the origin as the one derived from the measured beam patterns (4.72 mm for the feed horn beam and 8.28 mm for the beam generated by the QO feed chain). It should be noted that the modeling in Section 2 and calculations of the parameters of the test setup in Fig. 8(a) imply a 9 mm beam waist at the device aperture, whereas the smaller value, 8.28 mm, has been retrieved from the measured beam pattern. The discrepancy can be attributed to the thin-lens approximation used in Gaussian beam transformation as well as different excitations between the simulation and measurement.

In the case of the feed horn beam pattern, four polynomial terms with real-valued coefficients provided an excellent fit, whereas for the beam generated by the QO feed network and reflected off the pupil back (mirror) side, the polynomial coefficients had to be made complex valued; see Fig. 10(a). The FEA-simulated beam pattern in Fig. 10(a), corresponding to the reflection of the fundamental-mode Gaussian beam, with 8.28 mm beam waist at the pupil center from the device back (mirror) side, appears to be in a good agreement with measurements within the scan angle range of $\pm 8°$. This angular range permits fairly accurate analysis using the model of the fundamental-mode Gaussian beam ("GB0").

The plot in Fig. 10(b) shows the comparison of the Gaussian and ultra-Gaussian beams transmitted through the equivalent 60 mm transmissive pupil using the pupil model [Eq. (2)] and the beam model [Eq. (3)]. The ultra-Gaussian beam features almost the same FWHM and just ~1 dB increase of the nearest sidelobe level relative to the Gaussian beam. Therefore, this modelling supports the choice of the fundamental-mode Gaussian beam source for computationally efficient FEA simulations of the pupil performance with moderate effect on the results, instead of simulating the complicated QO feed chain.

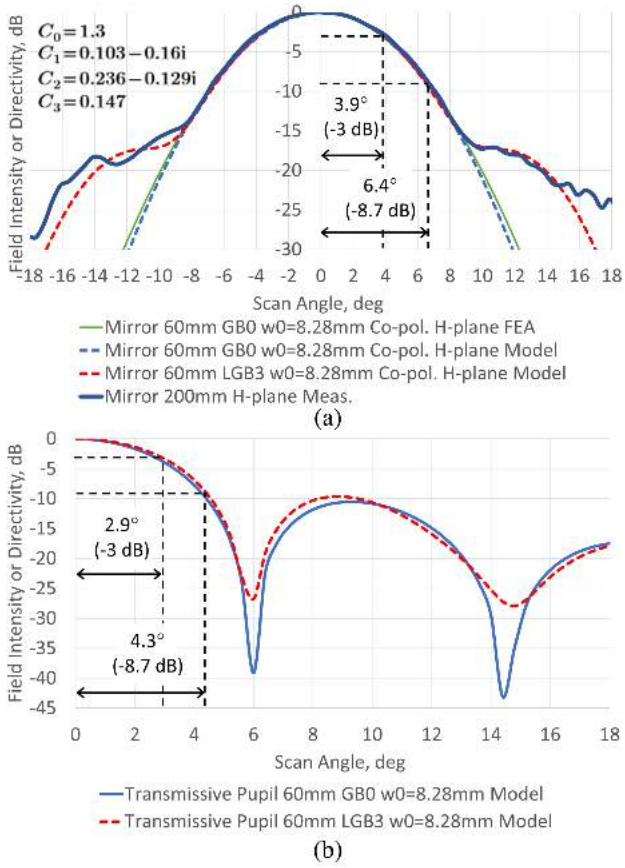

Fig. 10. Characterization of the source beam illuminating the reflective Toraldo pupil at 100 GHz by measurement, FEA simulation, and modeling with Eqs. (2) and (3): (a) measured source beam reflected from the pupil back (mirror) side, FEA simulation and model patterns of Gaussian (GB0) and ultra-Gaussian (LGB3) beams transmitted through a 60 mm circular aperture (adjusted beam waist of 8.28 mm) with the best-fit LGB coefficients [Eq. (3)] shown top left; (b) comparison of the model Gaussian and ultra-Gaussian beams transmitted through the 60 mm pupil. The figures of −3 dB and −8.7 dB correspond to the half-width at half-maximum and the beam width at $1/e^2$ of the maximum, respectively.

The H-plane beam measurements of the fabricated pupil were conducted in vertical polarization, as the DUTs with the attached QO feed chain were rotated in the horizontal plane about the DUT center (which was supposed to coincide with the phase center). The distance from the center of rotation to the probe was set to 500 mm, which was essentially constrained by the counterbalancing length of the rotating arm on which the components were mounted. By rotating the QO feed plus DUT assembly the fixed receiving probe scanned in the azimuthal plane, the spherical phase front of the Gaussian beam reflected off the DUT. The aperture-averaging effect of the probe was found to be negligible. Additional pyramidal and sheet radiation-absorbent materials (RAM) were used at places to reduce the unwanted scattering from the supporting structures.

C. Reflective Toraldo Pupil Measurement Results

The H-plane beam-measurement results for the patterned side of the reflective pupil are shown in Fig. 11 at 100 GHz. Compared with the beam pattern for the reflection from the mirror [Fig. 10(a)], the measurements demonstrate ∼42% reduction of the FWHM induced by the pupil. The measured nearest sidelobe level is less than −10 dB. These figures correspond well with the design values derived with Eq. (2) (see Fig. 4), although the FEA simulated beam profile (the green dashed curve in Fig. 11) appeared to be noticeably wider and exhibited a different structure of the sidelobes as compared with the experiment.

One obvious contribution to the above discrepancy is due to the use of the GB0 excitation in the FEA model, which proved to be valid only in a limited angular range for specular reflection [see Fig. 10(a)]. With respect to other possible effects, our FEA parametric analysis suggested that the discrepancy cannot be satisfactorily explained by reasonable deviation of the material parameters, the fabrication tolerances, or by a smaller source beam waist. However, by examining the beam pattern taken at a tilt angle with respect to the reference H plane (see the solid orange line in Fig. 11), we observed that the beam-pattern cut at 3.6° provides a good fit to the measurements within ± 6° scan angle range, which thus suggests that there might have been some inaccuracy in mounting the sample for reflection measurements. If that is true, reduction of the beam width by the pupil, according to the FEA simulations, recedes to ∼32%, which is even close to 25% value by design. It should also be noted in this respect that the sample warping during the measurements, as well as imperfect alignment of the components of the QO feed chain, may constitute another cause of the discrepancy.

Nonetheless, the measurements appeared to be in reasonably good quantitative agreement with prediction of the first-order diffraction model and FEA simulations, which thus provides evidence of the utility of the proposed design approach. Besides, our preliminary simulations of the complete test setup, including the corrugated feed horn, reimaging lens, and reflective pupil, using Altair FEKO electromagnetic simulation software [31] have confirmed that the super-resolution was attained. These simulations, along with new field-test results, will be reported in our future publication. In the future, we also intend to adopt the more accurate Kirchhoff or Rayleigh–Sommerfeld formulae at oblique incidence [27] for the reflective pupil modeling andthus eliminate the last equivalence in Fig. 3(e). This should allow more efficient design of eccentric coronae reflective pupils with improved beam symmetry; see, e.g., [32].

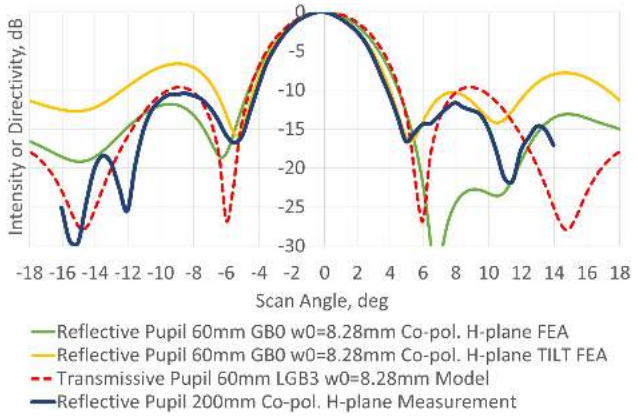

Fig. 11. Normalized beam patterns of the reflective Toraldo pupil at 100 GHz: measured (solid blue), FEA simulated (solid green for aligned and solid orange for tilted device), and calculated from the first-order diffraction model [Eqs. (2) and (3)], [dashed red, same as in Fig. 10(b)].

As to the optical performance of the reflective pupils, aimed to demonstrate super-resolution at millimeter wavelengths, we can conclude that despite the constraints of the FEA simulations (i.e., the use of the fundamental-mode Gaussian field source) and some paucity of experimental data (i.e., the lack of E-plane co-polarization and cross-polarization measurements, which were not possible with the available equipment), the presented results confirm the effect of diffractive beam narrowing in reflection.

4. CONCLUSIONS

The new concept of the reflective pupil based on the Toraldo super-resolution principle has been presented. The reflective pupil design procedure has been derived from first principles using the scalar theory of diffraction and the equivalence between reflective and transmissive structures. The fundamental trade-offs of the diffractive super-resolution have been discussed. Practical implementation of the reflective pupil structure has been developed using the working principle of the magnetic mirror presented in [25].

The beam shaping with the reflective pupil has been analyzed using the first-order diffraction model and FEA simulations with Ansys HFSS software. The reflective pupil device has been fabricated and measured with a quasi-optical setup. The test results proved to be in good quantitative agreement with simulations. Therefore, we have demonstrated the super-resolution achieved with the reflected pupil as well as the utility of the analytical and numerical modelling in the design of the reflective pupil.

More results of the experimental characterization will be reported elsewhere, including the E-plane beam measurements and cross-polarization data. Field tests of the reflective pupil in a millimeter-wave telescope are envisioned as well. Concerning the future concept developments, the use of broadband metal-mesh metamaterials can open new routes to the design of reflective pupils with arbitrary continuous phase and amplitude apodization, which thus permits three-dimensional, i.e., simultaneous transversal and longitudinal, super-resolution and ultimate control of the device performance.

Funding. Science and Technology Facilities Council (ST/N000706/1).

Disclosures. The authors declare no conflicts of interest.

REFERENCES

1. W. S. Holland, D. Bintley, E. L. Chapin, A. Chrysostomou, G. R. Davis, J. T. Dempsey, W. D. Duncan, M. Fich, P. Friberg, M. Halpern, K. D. Irwin, T. Jenness, B. D. Kelly, M. J. MacIntosh, E. I. Robson, D. Scott, P. A. R. Ade, E. Atad-Ettedgui, D. S. Berry, S. C. Craig, X. Gao, A. G. Gibb, G. C. Hilton, M. I. Hollister, J. B. Kycia, D. W. Lunney, H. McGregor, D. Montgomery, W. Parkes, R. P. J. Tilanus, J. N. Ullom, C. A. Walther, A. J. Walton, A. L. Woodcraft, M. Amiri, D. Atkinson,

B. Burger, T. Chuter, I. M. Coulson, W. B. Doriese, C. Dunare, F. Economou, M. D. Niemack, H. A. L. Parsons, C. D. Reintsema, B. Sibthorpe, I. Smail, R. Sudiwala, and H. S. Thomas, "SCUBA-2: the 10 000 pixel bolometer camera on the James Clerk Maxwell telescope," Mon. Not. R. Astron. Soc. **430**, 2513–2533 (2013).
2. T. Brien, P. Ade, P. Barry, E. Castillo, D. Ferrusca, T. Gascard, V. Gomez, P. Hargrave, A. Hornsby, D. Hughes, E. Pascale, J. Parrianen, A. Perez, S. Rowe, C. Tucker, S. V. González, and S. Doyle, "MUSCAT: the Mexico-UK Sub-Millimetre Camera for AsTronomy," Proc. SPIE **10708**, 107080M (2018).
3. J. Austermann, J. Beall, S. A. Bryan, B. Dober, J. Gao, G. Hilton, J. Hubmayr, P. Mauskopf, C. McKenney, S. M. Simon, J. Ullom, M. Vissers, and G. W. Wilson, "Large format arrays of kinetic inductance detectors for the TolTEC millimeter-wave imaging polarimeter," Proc. SPIE **10708**, 107080U (2018).
4. Y. Wen, K. Wang, and D. Kuang, "Improvement of telescope resolution using a diffractive phase modulator," Sci. Rep. **9**, 3475 (2019).
5. A. Carlotti, R. Vanderbei, and N. J. Kasdin, "Optimal pupil apodizations of arbitrary apertures for high-contrast imaging," Opt. Express **19**, 26796–26809 (2011).
6. C. J. R. Sheppard, "Fundamentals of superresolution," Micron **38**, 165–169 (2006).
7. G. T. di Francia, "Nuove pupille superrisolventi," Atti Fond. Giorgio Ronchi **7**, 366–372 (1952).
8. L. Olmi, P. Bolli, L. Cresci, F. D'Agostino, M. Migliozzi, D. Mugnai, E. Natale, R. Nesti, D. Panella, and L. Stefani, "Laboratory measurements of super-resolving Toraldo pupils for radio astronomical applications," Exp. Astron. **43**, 285–309 (2017).
9. D. Mugnai, A. Ranfagni, and R. Ruggeri, "Pupils with superresolution," Phys. Lett. A **311**, 77–81 (2003).
10. L. Olmi, P. Bolli, and D. Mugnai, "Design of discrete and continuous superresolving Toraldo pupils in the microwave range," Appl. Opt. **57**, 2215–2222 (2018).
11. G. Pisano, A. Shitvov, C. Tucker, D. Mugnai, P. Bolli, L. Olmi, F. D'Agostino, M. Migliozzi, A. Orfei, A. Navarrini, C. Riminesi, and B. Maffei, "Metamaterial-based Toraldo pupils for super-resolution at millimetre wavelengths," Proc. SPIE **10708**, 107080G (2018).
12. T. R. M. Sales and G. M. Morris, "Diffractive superresolution elements," J. Opt. Soc. Am. A **14**, 1637–1646 (1997).
13. T. Asakura and H. Mishina, "Diffraction by circular apertures with a ring-shaped π-phase change," Jpn. J. Appl. Phys. **9**, 195–202 (1970).
14. T. R. M. Sales and G. M. Morris, "Axial superresolution with phase-only pupil filters," Opt. Commun. **156**, 227–230 (1998).
15. M. Martínez-Corral, M. T. Caballero, E. H. K. Stelzer, and J. Swoger, "Tailoring the axial shape of the point spread function using the Toraldo concept," Opt. Express **10**, 98–103 (2002).
16. D. Roychowdhury, K. Bhattacharya, and A. K. Chakraborty, "Polarization phase in aberration compensation," Micron **38**, 158–164 (2007).
17. Q. Meng, J. Dong, D. Wang, and W. Liang, "Off-axis two-mirror system with wide field of view based on diffractive mirror," J. Opt. Soc. Korea **19**, 604–613 (2015).
18. D. P. Ghai, P. Senthilkumaran, and R. Sirohi, "Adaptive helical mirror for generation of optical phase singularity," Appl. Opt. **47**, 1378–1383 (2008).
19. A. Díaz-Rubio, V. S. Asadchy, A. Elsakka, and S. A. Tretyakov, "From the generalized reflection law to the realization of perfect anomalous reflectors," Sci. Adv. **3**, e1602714 (2017).
20. J. Scheuer, "Metasurfaces-based holography and beam shaping: engineering the phase profile of light," Nanophotonics **6**, 137–152 (2017).
21. Y. C. Cheng, S. Kicas, J. Trull, M. Peckus, C. Cojocaru, R. Vilaseca, R. Drazdys, and K. Staliunas, "Flat focusing mirror," Sci. Rep. **4**, 6326 (2014).
22. M. Born and E. Wolf, *Principles of Optics* (Oxford, Pergamon, 1975).
23. C. Rivolta, "Annular circular aperture: intensity maxima and minima on the optical axis," Appl. Opt. **27**, 922–925 (1988).
24. A. Roy, P. A. R. Ade, J. J. Bock, C. M. Brunt, E. L. Chapin, M. J. Devlin, S. R. Dicker, K. France, A. G. Gibb, M. Griffin, J. O. Gundersen, M. Halpern, P. C. Hargrave, D. H. Hughes, J. Klein, G. Marsden, P. G. Martin, P. Mauskopf, C. B. Netterfield, L. Olmi, G. Patanchon, M. Rex, D. Scott, C. Semisch, M. D. P. Truch, C. Tucker, G. S. Tucker, M. P. Viero, and D. V. Wiebe, "Deconvolution of images from BLAST 2005: insight into the K3-50 and IC 5146 star forming regions," Astrophys. J. **730**, 142 (2011).
25. G. Pisano, P. A. R. Ade, and C. Tucker, "Experimental realization of an achromatic magnetic mirror based on metamaterials," Appl. Opt. **55**, 4814–4819 (2016).
26. "Ansys HFSS—3D electromagnetic field simulator for RF and wireless design," www.ansys.com/products/electronics/ansys-hfss.
27. L. Zurak, V. Labinac, N. Erceg, I. Aviani, M. Jusup, and M. Karuza, "Testing scalar diffraction theory: Gaussian beam on a slit," J. Opt. Soc. Am. A **37**, 752–758 (2020).
28. B. Maffei, E. Gleeson, J. A. Murphy, and G. Pisano, "Study of corrugated Winston horns," Proc. SPIE **5498**, 812–817 (2004).
29. P. F. Goldsmith, *Quasioptical Systems: Gaussian Beam Quasioptical Propagation and Applications* (IEEE Press/Chapman & Hall, 1998), Chap. 3.
30. R. J. Wylde and D. H. Martin, "Gaussian beam-mode analysis and phase-centers of corrugated feed horns," IEEE Trans. Microw. Theory Tech. **41**, 1691–1699 (1993).
31. Altair Feko, https://altairhyperworks.com/product/FEKO.
32. T. Shiono and H. Ogawa, "Diffraction-limited blazed reflection diffractive microlenses for oblique incidence fabricated by electron-beam lithography," Appl. Opt. **30**, 3643–3649 (1991).